Applications in Engineering Science 5 (2021) 100034

Contents lists available at ScienceDirect

Applications in Engineering Science

journal homepage: www.elsevier.com/locate/apples

Turing-Hopf patterns in a morphochemical model for electrodeposition with cross-diffusion

Deborah Lacitignola [a,*], Ivonne Sgura [b], Benedetto Bozzini [c]

[a] Dipartimento di Ingegneria Elettrica e dell'Informazione, Università di Cassino e del Lazio Meridionale, via Di Biasio, I-03043 Cassino, Italy
[b] Dipartimento di Matematica e Fisica "Ennio De Giorgi", Università del Salento, via per Arnesano, I-73100 Lecce, Italy
[c] Dipartimento di Energia, Politecnico di Milano, via Lambruschini 4, Milano 20156, Italy

ARTICLE INFO

Keywords:
Pattern formation
Cross-diffusion
Turing-Hopf instability
ADI method
Finite differences
Battery modeling

ABSTRACT

This paper focuses on the impact of cross-diffusion for Turing-Hopf instability in a morphochemical model for electrodeposition (DIB) and completes the analysis on the role of cross-diffusion on pattern formation in electrodeposition we recently carried out in [Lacitignola et al. 2018]. We derive and discuss conditions for the destabilization *á la Turing* of the Hopf limit cycle in the neighborhood of the codimension-two Turing-Hopf bifurcation point, resulting in oscillatory Turing patterns. Numerical validation of the above theoretical findings is provided both in the case of Weak and Strong Turing-Hopf instability. Experimental evidence of this kind of phenomenology is then discussed also in relation to the charging and discharging process of a battery.

1. Introduction

Turing patterns appear in reaction-diffusion systems via Turing instability, a mechanism that can lead to spatial pattern formation when a homogeneous steady state which is stable in the absence of diffusion becomes unstable to an infinitesimal perturbation when diffusion is considered (Turing, 1952). It is based on Turing's revolutionary intuition that the interplay of two stabilizing processes can cause instability and lead to the arising of spatial structures. Turing's diffusion-driven instability is now universally recognized as one of the leading mechanisms of spatial self-organization in reaction-diffusion systems and boasts a large number of applications in many different fields, see e.g. Cross and Greenside (2009) and Sherratt (2012). Over the years, several generalizations of the reaction-diffusion theory for pattern formation have been undertaken in order to increase the complexity of the Turing's paradigm and drive the systems towards higher degree of realism. Among them, cross-diffusion has been widely used in reaction-diffusion models within the chemical, biological and environmental framework. Cross-diffusion refers to the phenomenon in which a flux of one species is induced by a gradient of another species. Such process can be characterized by the Fickian diffusivity matrix, whose off-diagonal elements are not both zero and can be either positive or negative. From a theoretical point of view, the analysis of reaction-diffusion systems with cross-diffusion can be a challenging task. Complications can arise from the strong nonlinear coupling and because the diffusion matrix may be neither symmetric nor in general positive definite such that even the local existence of solutions is far from being trivial. A well known assumption to prove - at least locally - existence of solutions is in fact that the diffusion matrix is positive definite, see e.g. Amann (1990) and Smoller (1994).

In addition, a large number of theoretical papers have analyzed the effects of cross-diffusion on Turing pattern formation and discussed its importance for the occurrence and understanding of the many types of patterns found in these systems. For example cross-diffusion can promote pattern formation even through small or negative cross-diffusion coefficients (Chattopadhyay and Tapaswi, 1997; Vanag and Epstein, 2009) or, when cross-diffusion is involved, nonlinearity in the source terms becomes not necessary for pattern formation to occur (Wang and Cai, 2013). Moreover, cross-diffusion driven instability conditions are a generalization of the classical conditions for Turing instability without cross-diffusion and the activator-inhibitor mechanism is no longer a necessary premise for pattern formation since activator-activator, inhibitor-inhibitor reaction kinetics as well as short-range inhibition and long-range activation have the same potential to promote cross-diffusion-driven instability (Madzvamuse and Barreira, 2014; Madzvamuse et al., 2015). Cross-diffusion also has a clear role into influencing the occurrence of supercritical or subcritical Turing instability, as recently shown in Gambino et al. (2016) by using the weakly nonlinear multiple scales analysis.

In Lacitignola et al. (2018), the effects of cross-diffusion on Turing pattern formation and selection were investigated for a morphochemical electrodeposition model introduced in Bozzini et al. (2013) and called DIB as an acronym by the authors' names. In electrodeposition processes

* Corresponding author.
E-mail addresses: d.lacitignola@unicas.it (D. Lacitignola), ivonne.sgura@unisalento.it (I. Sgura), benedetto.bozzini@polimi.it (B. Bozzini).

https://doi.org/10.1016/j.apples.2020.100034
Received 30 October 2020; Received in revised form 17 December 2020; Accepted 27 December 2020
Available online 29 December 2020

the morphological features - described by the DIB solution η - and the adsorbates that interact with the phase-formation process - quantified with solution θ - can cross-diffuse in a range of modes, corresponding to different real values of the cross-diffusion coefficients d_η and d_θ. To be more precise but without exhausting this topic that deserves more insightful theoretical and experimental analysis, the most representative scenarios can be outlined as follows. (i) Steps of crystalline metal surfaces - typical structural units that can be modelled by η - diffuse on the electrode, dragging adsorbates, that, in addition, can independently diffuse on the crystalline terraces, separated by steps. This physical condition can be described with $d_\theta = 0$, $d_\eta > 0$. (ii) If adsorbates (θ) strongly complex the surface metal atoms forming the steps, loosening their bonding to the metal substrate, the geometry of a step can change from a well-defined line, following the crystal structure, to a blurred one, resulting from a fluctuation of the position of the atoms at the step. In this case, diffusing adsorbates (θ) haul sections of steps, represented by η. This experimental situation can be described by $d_\theta > 0$. If steps also flow, then, $d_\eta > 0$, while, if they fluctuate around an average position that is constant in space, $d_\eta = 0$. Because of the considerable interest that the two subcases $d_\eta = 0$ or $d_\theta = 0$ have from an experimental point of view, in this paper we specifically focus on them, postponing the complete case $d_\eta \neq 0$ and $d_\theta \neq 0$ to future investigations.

The DIB spatio-temporal dynamics in the absence of cross-diffusion was extensively investigated in Bozzini et al. (2015); Lacitignola et al. (2017, 2014, 2015) revealing that it can undergo to Turing's diffusion-driven instability and that it can exhibit a variety of spatio-temporal phenomena, including also oscillatory inhomogeneous patterns caused by the interplay between Turing and Hopf instabilities. The Turing-Hopf interaction can take place either due to different competing bifurcations of multiple stationary states (De Wit, 1999) or through a codimension-two Turing-Hopf bifurcation (De Wit et al., 1996; Rudovics et al., 1996). However, as for the DIB model (Lacitignola et al., 2015), the spatio-temporal phenomenology in the neighborhood of a codimension-two TH point can be further enriched with the destabilization *á la Turing* of a Hopf limit cycle. In Ricard and Mischler (2009), this different way in which Turing and Hopf instabilities can interact is referred to as Turing-Hopf instability and involve the interesting problem of understanding how the oscillations of the stable limit cycle can impact the formation of diffusive instabilities in a reaction-diffusion model. In this paper, as in Lacitignola et al. (2015), we consider Turing-Hopf instability in this latter sense.

In Lacitignola et al. (2018), we found that the DIB model with negative cross-diffusion in the morphological elements as well as positive cross-diffusion in the surface chemistry is able to produce larger Turing parameter spaces and favor a tendency to stripeness that is not found in the case without cross-diffusion. However, the possible impact of cross-diffusion on Turing-Hopf instability was not addressed. This is the key contribution of the present paper.

2. The DIB model with cross-diffusion

The DIB model (Bozzini et al., 2013) with cross-diffusion is given by:

$$\begin{aligned}\frac{\partial \eta}{\partial t} &= \Delta\eta + d_\theta\,\Delta\theta + \rho\, f(\eta,\theta),\\ \frac{\partial \theta}{\partial t} &= d\,\Delta\theta + d_\eta\,\Delta\eta + \rho\, g(\eta,\theta).\end{aligned} \tag{1}$$

defined for $(x,y)\in\Omega=\left[0,L_x\right]\times\left[0,L_y\right]$, with initial conditions $\eta(x,y,0)=\eta_0(x,y)$, $\theta(x,y,0)=\theta_0(x,y)$, with $(x,y)\in\Omega$ and zero-flux boundary conditions on $\partial\Omega$. The variable $\eta(x,y,t)\in\mathbb{R}$ expresses the displacement from the instantaneous average electrodeposit plane whereas $0\le\theta(x,y,t)\le 1$ is the surface coverage with the functionally crucial adsorbate. The parameter d accounts for self-diffusion, being the ratio of the diffusion coefficients for the individual chemical and morphological processes, respectively; d_η and d_θ are the cross-diffusion coefficients that describe the flux of a variable due to the concentration gradient of the other variable; ρ can be interpreted as proportional to the area of the spatial 2D domain or as the relative strength of the reaction terms, Murray (2003). The nonlinear reaction terms f and g, given by

$$f(\eta,\theta) = A_1(1-\theta)\eta - A_2\eta^3 - B(\theta-\alpha), \tag{2a}$$

$$g(\eta,\theta) = C\left(1+k_2\,\eta\right)(1-\theta)[1-\gamma\,(1-\theta)] - D\left[\theta(1+\gamma\theta)+k_3\eta\theta(1+\gamma\theta)\right], \tag{2b}$$

account for the generation (deposition) and the loss (corrosion) of the relevant material. In the source term (2a): $A_1(1-\theta)\eta$ accounts for the charge-transfer rate at sites free from adsorbates; $A_2\eta^3$ describes mass-transport limitations to the electrodeposition process; $-B(\theta-\alpha)$ quantifies the effect of adsorbates on the electrodeposition rate; the parameter $0<\alpha\le 1$ accounts for the fact that adsorbates can have both inhibiting and enhancing effects on the growth rate. The source term (2b) can be regarded as $g(\eta,\theta) = C\,g_{ads}(\eta,\theta) - D\,g_{des}(\eta,\theta)$ and features adsorption (parameter C) and desorption (parameter D) terms including both chemical and electrochemical contributions. Further details about the physico-chemical meaning of the source terms are extensively provided in Bozzini et al. (2013).

Without loss of generality, we assume that: (i) except for the cross-diffusion coefficients, all the other constants are taken as real positive or equal to zero, with α and $\gamma\in(0,1)$; (ii) $k_3<k_2$, meaning that adsorption is the dominating chemical contribution to growth; (iii) the following relation holds:

$$D = \frac{C(1-\alpha)(1-\gamma+\gamma\alpha)}{\alpha(1+\gamma\alpha)} \tag{3}$$

so that the adsorption and desorption rates are proportional ($D\propto C$).

As discussed in Lacitignola et al. (2015), the source terms (2a)-(2b) with condition (3) allow model (1) to support a multiplicity of spatially uniform equilibria, whose number and numerical values are not dependent on the parameter C. Among them, it is particularly interesting to focus on the equilibrium $P_e=(\eta_e,\theta_e)=(0,\alpha)$ that is a spatially independent equilibrium for any choice of the parameter values and corresponds to a flat electrode surface from which morphologies can develop. In Lacitignola et al. (2015), by considering B and C as bifurcation parameters, we found that in the spatially uniform case P_e can loose its stability either by transcritical or by Hopf bifurcation. Conditions

$$B = B_{tr} = \frac{A_1\,(1-\alpha)\,F_2(\alpha,\gamma)}{(k_2-k_3)\,F_1(\alpha,\gamma)}, \tag{4}$$

and

$$C = C_{hopf} = \frac{A_1\,(1-\alpha)}{F_2(\alpha,\gamma)}, \qquad B > B_{tr}, \tag{5}$$

with

$$F_1(\alpha,\gamma) = (1-\alpha)(1-\gamma+\alpha\gamma); \qquad F_2(\alpha,\gamma) = \frac{2\alpha\gamma(1+\alpha\gamma-\gamma)+1-\gamma}{\alpha(1+\alpha\gamma)}, \tag{6}$$

are respectively the transcritical and the Hopf bifurcation thresholds. We stress that, holding the assumptions on the parameters α and γ, both $F_1(\alpha,\gamma)$ and $F_2(\alpha,\gamma)$ are positive quantities.

In the spatial case without cross-diffusion, we proved - through linear stability (Lacitignola et al., 2015) and weakly nonlinear stability (Bozzini et al., 2015) analysis - that P_e can experience Turing instability and that both the Turing and the Turing-Hopf instabilities can be responsible for the emergence of spatio-temporal organization in model (1)–(2). In Lacitignola et al. (2018), we investigated the effects of cross-diffusion on Turing pattern formation. Here, we want to explore how Turing-Hopf patterns can be affected by the cross-diffusion mechanism. To this aim, we start by recalling conditions - derived in Lacitignola et al. (2018) - for the emergence of Turing patterns in the DIB model with cross-diffusion and show the impact of cross-diffusion

on the Turing parameter space. We preliminary stress that a reaction-diffusion system is said to exhibit Turing instability driven by both diffusion and cross-diffusion if a spatially uniform steady state - that is locally *stable* in the absence of diffusion and cross-diffusion - becomes *unstable* to small spatial perturbations when diffusion and cross-diffusion are present Madzvamuse et al. (2015).

3. Cross-Diffusion and Turing parameter space

The DIB model with cross-diffusion (1)-(2) can be equivalently expressed as:

$$\frac{\partial w}{\partial t} = \widetilde{D}\Delta w + \rho\, S(w) \tag{7}$$

with zero flux boundary conditions on Ω, where

$$w = \begin{pmatrix}\eta\\ \theta\end{pmatrix}, \qquad \widetilde{D} = \begin{pmatrix}1 & d_\theta\\ d_\eta & d\end{pmatrix}, \qquad S = \begin{pmatrix}f(\eta,\theta)\\ g(\eta,\theta)\end{pmatrix},$$

i.e. w contains the system variables, $\tilde{D}$ contains the diffusion and cross-diffusion coefficients and S accounts for the reaction kinetics. The diffusion matrix $\tilde{D}$ must satisfy $det(\tilde{D}) > 0$ for the system to be well posed (Miller et al., 1986; Mutoru and Firoozabadi, 2011; Vanag and Epstein, 2009), i.e.

$$d - d_\eta\, d_\theta > 0. \tag{8}$$

The stability of the homogeneous equilibrium $P_e = (\eta_e, \theta_e) = (0, \alpha)$ is obtained by studying the behavior of the system when a small inhomogeneous perturbation δw

$$\delta w(\mathbf{z}, t) = \sum_k c_k e^{\sigma_k t} U_k(\mathbf{z}), \tag{9}$$

is introduced in the neighborhood of w_e, i.e. $w = w_e + \delta w$. In (9), the $U_k(\mathbf{z})$ are the spatial eigenfunctions associated with the spatial eigenvalues λ_k, with $k \in \mathbb{N}$, of the unbounded non-negative linear operator $-\Delta$ with zero-flux boundary conditions on $\partial\Omega$. We also observe that, since $\Omega = [0, L_x] \times [0, L_y]$, and recalling that the spatial variable $\mathbf{z}$ is $\mathbf{z} = (x, y)$ and the wave number $\mathbf{k}$ is $\mathbf{k} = (k_x, k_y)$, the eigenfunction in (9) can be chosen as $U_k(\mathbf{z}) = \cos k_x\, x \cos k_y\, y$ where $k_j = p_j\, \pi / L_j$, for $p_j \in N$, $j = x, y$ and the related spatial eigenvalue λ_k turns out to be $\lambda_k = k^2$. The eigenvalues $\sigma = \sigma(\lambda_k)$ account for the temporal part and describe the growth rate of the perturbation. They are solutions of the second order algebraic equation:

$$\left|\rho\, J(P_e) - \lambda_k\, \widetilde{D} - \sigma\, I\right| = 0, \tag{10}$$

where I is the 2×2 identity matrix and $J(P_e)$ is the Jacobian matrix evaluated at the steady state P_e:

$$J(P_e) = \begin{pmatrix} A_1\,(1-\alpha) & -B\\ C(k_2 - k_3)\, F_1(\alpha,\gamma) & -C\, F_2(\alpha,\gamma)\end{pmatrix}, \tag{11}$$

with $F_i(\alpha, \gamma)$ given by (6). For a given λ_k, Turing instability occurs if Eq. (10) admits a solution σ such that $Re[\sigma(k^2)] > 0$ for some k^2 non-zero. By (10) hence follows that $\sigma(k^2)$ verifies the dispersion relation:

$$\sigma^2 + a(k^2)\,\sigma + h(k^2) = 0 \tag{12}$$

with

$$a(k^2) = k^2\,(1 + d) - \rho\,\tau_e, \qquad h(k^2) = \widetilde{\delta}\, k^4 - \rho\,(d\, J^e_{11} + J^e_{22} - d_\eta\, J^e_{12} - d_\theta\, J^e_{21})\, k^2 + \rho^2\, \delta_e,$$

and where the quantities $\tau_e, \delta_e, \widetilde{\delta}$ are defined as

$$\tau_e = tr(J(P_e)), \qquad \delta_e = det(J(P_e)), \qquad \widetilde{\delta} = det(\widetilde{D}). \tag{13}$$

The Turing space - consisting of parameters resulting in Turing instability - is hence bounded by the following set of inequalities:

$$\begin{aligned}
&\tau_e < 0 \quad \text{and} \quad \delta_e > 0,\\
&d\, J^e_{11} + J^e_{22} - d_\eta\, J^e_{12} - d_\theta\, J^e_{21} > 0,\\
&(d\, J^e_{11} + J^e_{22} - d_\eta\, J^e_{12} - d_\theta\, J^e_{21})^2 - 4\,\widetilde{\delta}\,\delta_e > 0,
\end{aligned} \tag{14}$$

where J^e_{ij} is the ij entry of the Jacobian matrix (11). The first inequality is derived by stability considerations on the homogeneous equilibrium P_e in the absence of diffusion and cross-diffusion, the others are obtained by considerations on the onset of instability when diffusion and cross-diffusion are introduced. We refer to Lacitignola et al. (2018) and references therein for the explicit derivation of (14).

By choosing B and C as bifurcation parameters and provided that the cross-diffusion coefficients satisfy the requirement (8), the general conditions (14) for Turing instability in the presence of cross-diffusion specialize to

$$\begin{aligned}
&B > A_1\,(1-\alpha)\, d_*\\
&C_{min} < C < \frac{d\, A_1\,(1-\alpha) + B\, d_\eta}{F_2(\alpha,\gamma) + d_\theta\, F_1(\alpha,\gamma)(k_2 - k_3)}\\
&a_2\, B^2 + a_1\, B + a_0 > 0,
\end{aligned} \tag{15}$$

where $C_{min} = C_{hopf}$ or $C_{min} = C_d$, with C_{hopf} defined in (5) and $C_d = \frac{d}{d-1}\, C_{hopf}$. The positive quantity d_* and the coefficients a_i, with $i = 0, 1, 2$, are instead given by:

$$d_* = \frac{F_2(\alpha,\gamma)}{F_1(\alpha,\gamma)(k_2 - k_3)}, \tag{16}$$

and

$$\begin{aligned}
a_2 &= \frac{d_\eta^2}{4\,(d - d_\eta\, d_\theta)},\\
a_1 &= \frac{d_\eta}{2(d - d_\eta\, d_\theta)}\left[A_1\, d\,(1-\alpha) - C\, F_2(\alpha,\gamma)\right]\\
&\quad - C\, F_1(\alpha,\gamma)\,(k_2 - k_3)\left[1 + \frac{d_\eta d_\theta}{2(d - d_\eta\, d_\theta)}\right],\\
a_0 &= \frac{\left[A_1\, d\,(1-\alpha) - C\, F_1(\alpha,\gamma)\, d_\theta\,(k_2 - k_3) - C\, F_2(\alpha,\gamma)\right]^2}{4\,(d - d_\eta\, d_\theta)}\\
&\quad + A_1\, C\, F_2(\alpha,\gamma)(1-\alpha).
\end{aligned} \tag{17}$$

In the next, we specifically focus on the case of cross-diffusion in one component only. For this case, conditions for the emergence of Turing patterns are provided in the following theorems (Lacitignola et al., 2018):

Theorem 3.1. *[case $d_\eta = 0, \forall d_\theta$]*

If $d_\eta = 0$ and $-d_* < d_\theta < d_*\,(d-1)$, then the set of inequalities (15)–(17), with $C_{min} = C_{hopf}$, locate a Turing region in the (C, B) parameter space.

Theorem 3.2. *[case $d_\theta = 0, \forall d_\eta$]*

(a) If $d_\theta = 0$ and $-\frac{(d-1)\,A_1(1-\alpha)}{B} < d_\eta < \frac{1}{d_*}$, then the set of inequalities (15)–(17) locate a Turing region in the (C, B) parameter space with $C_{min} = C_{hopf}$. (b) If $d_\theta = 0$ and $d_\eta > \frac{d}{d_*(d-1)}$, then the set of inequalities (15)–(17) locate a Turing region in the (C, B) parameter space with $C_{min} = C_d$.

The related bifurcation diagrams are depicted in Fig. 1 with the aim to show how cross-diffusion can impact the Turing parameter space so to elucidate its role in enhancing or inhibiting spatial pattern formation.

For the case of cross-diffusion in the η component only, i.e. $d_\eta = 0$, negative values of d_θ produce Turing parameter spaces larger than those obtained in the absence of cross-diffusion, whereas positive values of d_θ gives Turing parameter spaces that are progressively smaller than those found without cross-diffusion, Fig. 1(a). Differently, for the case of cross-diffusion in the θ component only, i.e. $d_\theta = 0$, positive values of d_η produce Turing parameter spaces that are considerably larger than those found in the absence of cross-diffusion whereas negative values of d_η produce Turing parameter spaces that are progressively smaller than those obtained without cross-diffusion, Fig. 1(b).

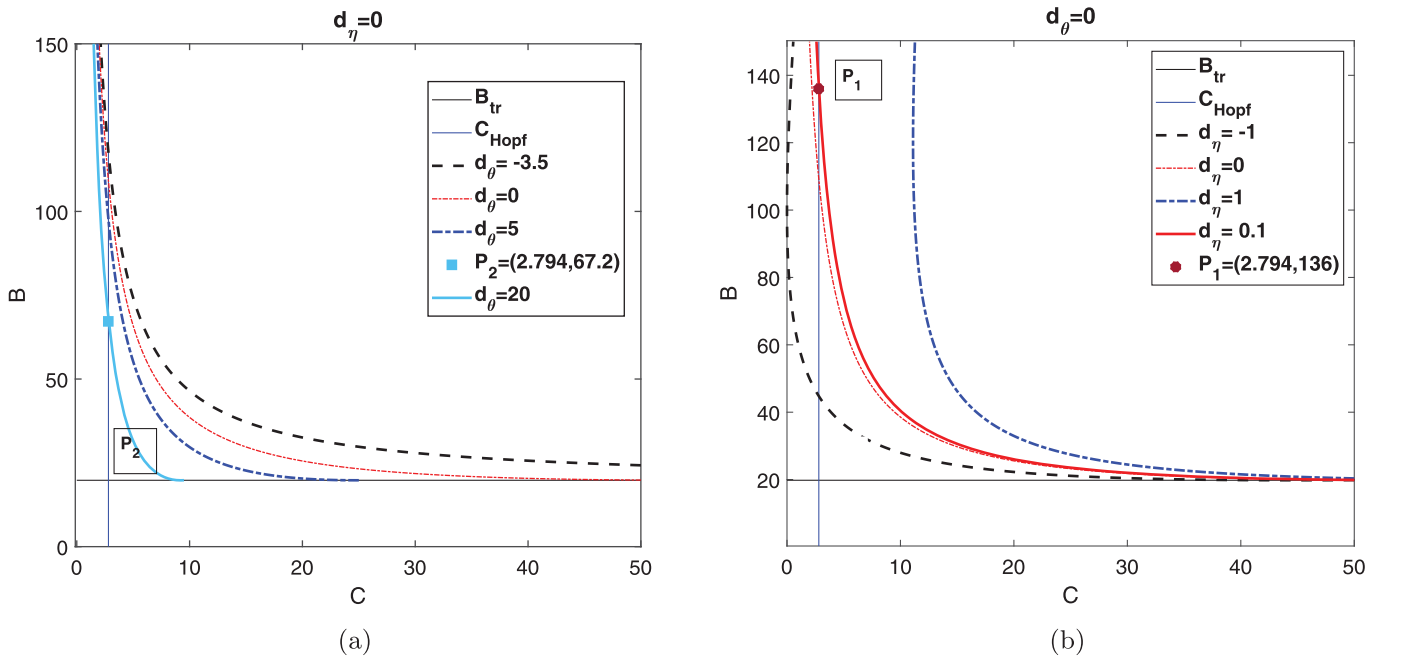

Fig. 1. Bifurcation diagram in the (C,B) parameter space. The other parameters in the DIB model are fixed as: $d = 20; \alpha = 0.5; \gamma = 0.2; k_2 = 2.5; k_3 = 1.5; A_1 = 10; A_2 = 30$. The vertical and horizontal straight lines are respectively the Hopf and the transcritical bifurcation lines; the curved lines are the Turing bifurcation curves. The Turing region is the area bounded by the Hopf, the transcritical and the Turing curves. The Turing-Hopf region corresponds to a neighbor of the intersection point between each Turing curve and the Hopf line. (a) Case $d_\eta = 0, d_\theta \neq 0$, cross-diffusion in the η component only: the Turing curves for $d_\theta = -3.5, 0, 5, 20$ are showed. For $d_\theta = 20$, the solid Turing curve and the point P_2 identify the TH region for the *weak* Turing-Hopf numerical simulations reported in Section 4.1. (b) Case $d_\theta = 0, d_\eta \neq 0$, cross-diffusion in the θ component only: the Turing curves for $d_\eta = -1, 0, 0.1, 1$ are showed. For $d_\eta = 0.1$, the solid Turing curve and the point P_1 identify the TH region for the *strong* Turing-Hopf numerical simulations reported in Section 4.1.

4. Cross-diffusion and Turing instability of the Hopf cycle

Inspired by the paper (Ricard and Mischler, 2009), in Lacitignola et al. (2015) we investigated the onset of diffusive instabilities of the spatially uniform limit cycle - generated by a supercritical Hopf bifurcation - for the electrodeposition model (1)-(2) without cross-diffusion. More precisely, we showed that this peculiar mechanism is responsible for the appearance of an interesting class of spatio-temporal patterns in the neighborhood of the codimension-two TH point. In this section we intend to show the effect of cross-diffusion on the emergence of such a phenomenology.

In Lacitignola et al. (2015) and Ricard and Mischler (2009) it was shown that there are essentially two ways in which the Hopf limit cycle can give rise to Turing instabilities near a TH point, that are defined as (i) weak and (ii) strong Turing-Hopf instabilities, respectively. Weak instabilities are characterized by dominant inhomogeneous steady patterns onto which slightly time periodic oscillations can be overlapped, exhibiting the same frequency as the limit cycle. Differently, strong instabilities are characterized by an intermittent switching between the inhomogeneous patterns and its *complementary pattern*. In this case, the oscillating spatial pattern and the Hopf cycle exhibit different frequencies.

To obtain conditions for the occurrence of Weak or Strong TH instabilities for model (1)-(2), we make use of Theorem 4.1, derived in Ricard and Mischler (2009), that also applies to a general reaction-diffusion model with cross-diffusion:

Theorem 4.1. *Ricard and Mischler (2009) Let λ_k be a positive spatial eigenvalue. Let τ_T and δ_T be defined as:*

$$\tau_T = \mathrm{tr}(J(\eta_e, \theta_e) - \lambda_k \tilde{D}), \qquad \delta_T = \det(J(\eta_e, \theta_e) - \lambda_k \tilde{D}).$$

Further assume that the reaction system has a limit cycle attained via a Hopf bifurcation. If $\tau_T \leq 0$ and $\delta_T < 0$ then weak TH instabilities appear. If $\tau_T > 0$, TH instabilities appear and they are weak provided $\tau_T^2 - 4\delta_T \geq 0$ while they are strong if $\tau_T^2 - 4\delta_T < 0$.

For the general reaction-diffusion system (7), the quantities τ_T and δ_T become:

$$\tau_T = \rho\,\tau_e - \lambda_k\,(1+d); \qquad \delta_T = \rho^2\,\delta_e + \lambda_k^2\,\widetilde{\delta} + \lambda_k\,\rho\left[d_\theta J^e_{21} + d_\eta J^e_{12} - J^e_{22} - d\,J^e_{11}\right]$$

where τ_e, δ_e, $\widetilde{\delta}$ are defined in (13). We recall that the occurrence of a stable limit cycle because of a supercritical Hopf bifurcation means that $0 < \tau_e \ll 1$. We also observe that, the positive values of λ_k for which $\delta_T < 0$ belong to the open interval $\Lambda = (\lambda_-, \lambda_+)$ with $\delta_T(\lambda_\pm) = 0$, where

$$\lambda_\pm = \frac{-\rho\,\zeta \pm \rho\sqrt{\zeta^2 - 4\,\delta_e\,\widetilde{\delta}}}{2\,\widetilde{\delta}}, \tag{18}$$

and $\zeta = d_\theta J^e_{21} + d_\eta J^e_{12} - J^e_{22} - d\,J^e_{11}$. In the following we assume, for the spatial domain $\Omega = [0, L_x] \times [0, L_y]$, that the non-dimensional lengths are such that $L_x \geq L_y$. Therefore, the smallest positive spatial eigenvalue is given by $\lambda_{(1,0)} = \pi^2/L_x^2$.

As observed before in Section 2, the electrodeposition model (1)-(2) experiences at $C = C_{hopf}$ a supercritical Hopf bifurcation such that a stable limit cycle can be found, surrounding the unstable uniform steady state P_e. As a consequence, it makes sense to investigate *if* and *how* cross-diffusion can impact the occurrence of the TH instability of this Hopf cycle. To this end, we consider the quantities τ_T and δ_T only as function of (i) the bifurcation parameters B and C, (ii) the diffusion and cross-diffusion coefficients d, d_η, d_θ, (iii) the scaling parameter ρ. The other parameters are fixed as in Fig. 1.

Let us define the following quantity as *effective domain size*, introduced and discussed in details in Lacitignola et al. (2017):

$$\mathcal{A} = \rho\,L_x^2.$$

Is easy to see that $\mathcal{A}$ is proportional to the geometric size of the domain of integration and ρ can indeed be regarded as a scaling parameter of

the surface area (Murray, 2003). From linear stability analysis, it also follows that - fixing all the other parameters - the range of wavenumbers yielding the arising of spatial patterns enlarges with increasing the size parameter ρ. This implies that more complex and structured patterns can be expected by increasing the value of $\mathcal{A}$.

In order to better characterize the emerging of TH instability, we choose to express the relevant quantities in Theorem 4.1 in terms of the effective domain size $\mathcal{A}$. We hence obtain:

$$\tau_T \leq 0 \quad \Leftrightarrow \quad \mathcal{A} \leq \frac{\pi^2 (1+d)}{\tau_e} \tag{19}$$

where $0 < \tau_e << 1$ and

$$\begin{aligned} &\delta_T < 0 \quad \Leftrightarrow \quad b_2 \mathcal{A}^2 + b_1 \mathcal{A} + b_0 < 0, \\ &\tau_T^2 - 4\,\delta_T < 0 \quad \Leftrightarrow \quad c_2 \mathcal{A}^2 + c_1 \mathcal{A} + c_0 < 0. \end{aligned} \tag{20}$$

where b_i and c_i, $i = 2, 1, 0$ are given respectively by

$$\begin{aligned} b_2 &= C\,(.45\,B - 8.9090), \\ b_1 &= \left(-49.3480\,d - 9.8696\,B\,d_\eta + 4.4413\,C\,d_\theta + 17.5858\,C\right), \\ b_0 &= 97.4090\left(d - d_\eta\,d_\theta\right). \end{aligned} \tag{21}$$

and

$$\begin{aligned} c_2 &= \left(25.00 + 17.8182\,C + 3.1749\,C^2 - 1.80\,C\,B\right), \\ c_1 &= (-98.6960 + 98.6960\,d - 35.1717\,C + 35.1717\,C\,d \\ &\quad + 39.4784\,B\,d_\eta - 17.7653\,C\,d_\theta), \\ c_0 &= \left[97.4091\,(1+d^2) - 194.8182\,d + 389.6364\,d_\eta\,d_\theta\right]. \end{aligned} \tag{22}$$

To explore the role of cross-diffusion for the possible destabilization *á la Turing* of the Hopf cycle, we fix $d = 20$ and consider the two cases: (A) cross-diffusion in the η component only, i.e. $d_\eta = 0$; (B) cross-diffusion in the θ component only, i.e. $d_\theta = 0$.

Case A: $d_\eta = 0$. We recall by Theorem 3.1 that the codimension 2 TH point - given by the intersection between the Hopf line and the Turing bifurcation curve - can be found for each value of d_θ such that $-d_* < d_\theta < d_*(d-1)$, where d_* is given in (16). For our choice of the parameters, we have $-3.9595 < d_\theta < 75.2329$ and the TH point is given by:

$$C_{TH} = C_{hopf} = \frac{A_1\,(1-\alpha)}{F_2(\alpha,\gamma)} = 2.8061, \quad B_{TH} = B_{TH}(d_\theta) \tag{23}$$

Fig. 2(a) shows how the value of B_{TH} decreases for increasing values of d_θ. In particular, for $d_\theta = 0$, we recover the TH point $(C_{TH}, B_{TH}) = (2.8061, 109.7979)$ found in Lacitignola et al. (2015) for the DIB model without cross-diffusion.

By increasing d_θ from negative to positive values, by Theorem 4.1 and (19)-(20), we conclude that Weak or Strong TH instabilities can be expected for the ranges of the parameter $\mathcal{A}$ summarized in Table 1. The last row in Table 1, i.e. the case $d_\theta = 20$ (shown in bold typing), corresponds to the Weak TH phenomenology reported in Section 4.1. We observe that, when the other parameters are fixed, to have Strong TH instability the effective domain size $\mathcal{A}$ must be greater than a threshold value that is independent on the value of d_θ but only depends on d and C. Instead, for the emergence of Weak TH instability, the ranges of $\mathcal{A}$ depend on d_θ and are bounded intervals whose size increases with increasing d_θ.

Case B: $d_\theta = 0$. By Theorem 3.2 it follows that the codimension-two TH point can be found only for $d_\eta \in [-4.5, 0.2525]$. We observe that in the (C, B) parameter space, with B verifying condition (5), the TH point is such that:

$$C_{TH} = C_{hopf} = \frac{A_1\,(1-\alpha)}{F_2(\alpha,\gamma)} = 2.8061, \quad B_{TH} = B_{TH}(d_\eta)$$

We report $B_{TH}(d_\eta)$ in Fig. 2(b). Also in this case, when $d_\theta = 0$, we find the TH point $(C_{TH}, B_{TH}) = (2.8061, 109.7979)$ found in Lacitignola et al. (2015) in the absence of cross-diffusion.

In the following, we shall consider decreasing values of the cross-diffusion coefficient d_η. By Theorem 4.1 and taking into account of (19)-(20), we conclude that Weak or Strong TH instabilities can be expected for ranges of the parameter $\mathcal{A}$ summarized in Table 2. The row in Table 2 for $d_\eta = 0.1$ (shown in bold typing) corresponds to the Strong TH phenomenology reported in Section 4.1.

Also in this case, when the other parameters are fixed, to have Strong TH instability the effective domain size $\mathcal{A}$ must be greater than a threshold value that is independent on the value of d_η. The ranges of $\mathcal{A}$ allowing for the Weak TH instability depends instead on d_η and are bounded intervals whose size becomes larger for decreasing values of d_η.

4.1. Numerical validation

To validate the above results we present numerical simulations for both the Weak and the Strong phenomenologies. Numerical simulation for model (1)-(2) with cross-diffusion have been obtained by the ADI-ECDF method described in detail in Sgura et al. (2012), Settanni and Sgura (2016). As in Lacitignola et al. (2018), this method approximates the new Laplace operators related to the cross-diffusion terms by finite differences with the same accuracy in space and the reaction terms are always approximated explicitly in time. The initial conditions $\eta_0(x, y) =$

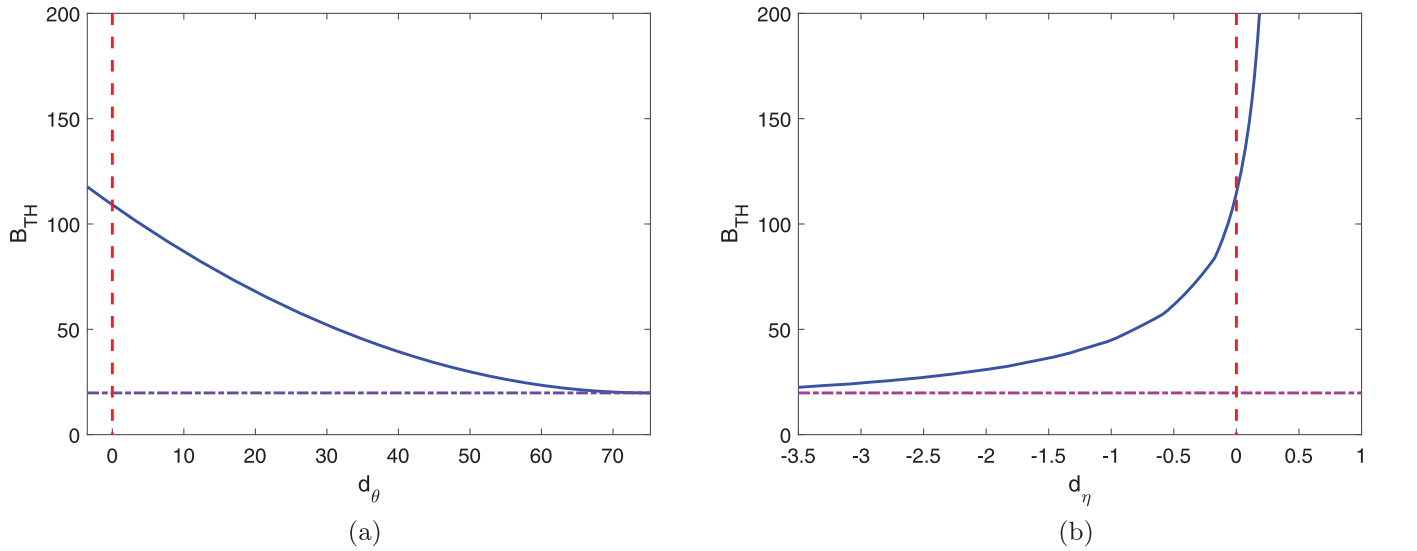

Fig. 2. (a) Cross-diffusion in η components only, i.e. $d_\eta = 0$. B_{TH} as a function of d_θ. (b) Cross-diffusion in θ components only, i.e. $d_\theta = 0$. B_{TH} as a function of d_η. The other parameters are fixed as in Fig. 1.

Table 1
Case A - $d_\eta = 0$. 1st and 2nd columns: cross-diffusion coefficient d_θ and corresponding codimension-two TH points. 3rd column: chosen point in the neighborhood of the TH point. 4th-5th columns: ranges of the effective domain size $\mathcal{A}$ for which Weak or Strong TH instabilities can be expected in the neighborhood of the TH point.

d_θ	(C_{TH}, B_{TH})	*(C, B) values*	*Weak TH*	*Strong TH*
-3.5	(2.8061, 117.6340)	(2.794, 117)	$\mathcal{A} \in (3.5953, 4.4339)$	$\mathcal{A} > 9595.4492$
1	(2.8061, 106.7779)	(2.794, 106)	$\mathcal{A} \in (3.7680, 4.7705)$	$\mathcal{A} > 9595.4492$
10	(2.8061, 86.9656)	(2.794, 86.2)	$\mathcal{A} \in (4.2292, 5.5176)$	$\mathcal{A} > 9595.4492$
20	(2.8061, 67.9508)	(2.794, 67.2)	$\mathcal{A} \in$ (**4.8989, 6.6725**)	$\mathcal{A} > 9595.4492$

Table 2
Case B - $d_\theta = 0$. 1st and 2nd columns: decreasing values of $d_\eta$and the corresponding codimension-two TH-points. 3rd column: chosen points in the neighborhood of the TH point. 4th-5th columns: Ranges of the parameter $\mathcal{A}$ for which Weak or Strong TH instabilities can be expected in the neighborhood of the TH point.

d_η	(C_{TH}, B_{TH})	*(C, B) values*	*Weak TH*	*Strong TH*
0.2525	(2.8061, 400.6875)	(2.794, 400)	$\mathcal{A} \in (1.8842, 2.1629)$	$\mathcal{A} > 9595.4492$
0.1	(2.8061, 136.6972)	(2.794, 136)	$\mathcal{A} \in (3.3137, 4.0241)$	$\mathcal{A} >$ **9595.4492**
-1	(2.8061, 44.7719)	(2.794, 44.2)	$\mathcal{A} \in (6.3519, 9.9968)$	$\mathcal{A} > 9595.4492$
-3.5	(2.8061, 22.4587)	(2.794, 22)	$\mathcal{A} \in (14.0070, 50.2370)$	$\mathcal{A} > 9595.4492$

$\eta_e + 10^{-5}$ rand(x, y), $\theta_0(x, y) = \theta_e + 10^{-5}$ rand(x, y) are uniformly random spatial perturbations of the homogeneous equilibrium P_e.

Weak TH instability.

To illustrate the phenomenology related to Weak TH instability in the neighborhood of the codimension-two bifurcation point (C_{TH}, B_{TH}), we choose the case of cross-diffusion in the η component only, Case A. According to our theoretical findings, in this case Turing-Hopf instability is possible for $-d_* < d_\theta < d_*(d-1)$ so that, for the chosen set of parameter values, $-3.9595 < d_\theta < 75.2323$. As a consequence, we set $d_\eta = 0$ and $d_\theta = 20$ and, since $(C_{TH}, B_{TH}) = (2.8061, 67.9508)$, we fix $C = 2.794$ and $B = 67.2$ corresponding to the values of the fourth row of Table 1, see also Fig. 1(a). We choose $L_x = 2$, $L_y = 1$ and $\rho = 1.6250$ so that $\mathcal{A} \in (4.8989, 6.6725)$. Table 1 hence suggests that weak TH instability is expected, associated with $\lambda_{(1,0)}$, implying the appearance of a dominant steady pattern slightly oscillating only in time with the same frequency of the limit cycle. This phenomenology is depicted in Fig. 3(a) where the 3D snapshots of the solution every $\Delta t = 20$ until $T_f = 180$ show that the asymptotic stationary spatial structure oscillates only in time. Fig. 3(b) shows instead the oscillating behavior of $\langle\eta(t)\rangle$ (left panel) and the corresponding limit cycle in the phase plane $(\langle\eta(t)\rangle, \langle\theta(t)\rangle)$ (right panel), where $\langle\eta(t)\rangle, \langle\theta(t)\rangle$ are the mean spatial values of the unknowns evolving in time. An asymptotic oscillating behavior of these approximated functions for long times will indicate that in the phase plane a limit cycle has been attained.

Strong TH instability.

We consider cross-diffusion in the θ component only, Case B, to show the emerging of Strong TH instability in the neighborhood of the codimension-two TH point. Our theoretical findings indicate that in this case Turing-Hopf instability is possible only for $d_\eta < 0.2525$ so that we set $d_\theta = 0$ and $d_\eta = 0.1$, corresponding to the values of the second row of Table 2. As a consequence, $(C_{TH}, B_{TH}) = (2.8061, 136.6972)$ and we fix $C = 2.794$ and $B = 136$, corresponding to the point P_1 in Fig. 1(b). We choose $L_x = 100$, $L_y = 70$ and $\rho = 50$ so that $\mathcal{A} > 9595.4492$. According to Table 2, strong TH instability is expected, associated with $\lambda_{(1,0)}$. This implies the appearance of an intermittent pattern whose theoretical frequency is $\sigma_i = \sqrt{\delta_T - \tau_T^2/4} = 604.3561$ that is different from the frequency $\omega_{cycle} = 529.9987$ of the limit cycle obtained via supercritical Hopf bifurcation. In Fig. 4(a) the 3D snapshots of the solution every $\Delta t = 0.2$ until $T_f = 1.8$ show that the spatial structure oscillates both in space and time. Fig. 4 (b) shows instead the oscillating behavior of the space mean integral $\langle\eta(t)\rangle$ (left panel) and the corresponding limit cycle in the phase plane $(\langle\eta(t)\rangle, \langle\theta(t)\rangle)$ (right panel). The symbols $'o'$ in Fig. 4(b), left, indicate the points $(t_i, \langle\eta(t_i)\rangle), i = 1, \ldots, 9$ corresponding to the patterns in Fig. 4(a) for the same time values. In particular, for $t = 1.2$ and $t = 1.4$, a maximum and a minimum in $\langle\eta(t_i)\rangle$ correspond to complementary patterns in Fig. 4(a), thus showing the Strong TH behavior of the solution.

5. Discussions and concluding remarks

In Lacitignola et al. (2018), with the aim to compare the dynamical properties of the DIB model with other reaction-diffusion systems found in literature and typically referring to biological phenomena, we discussed the DIB model within the activator-inhibitor framework. In fact the structure of the source terms of the DIB model, allowed us to classify it among the pure activator-inhibitor systems, with η the activator and θ the inhibitor. We found that when cross-diffusion in the activator only was considered ($d_\eta = 0$), negative cross-diffusion of the activator enhanced Turing instability driven by diffusion and cross-diffusion, by producing larger Turing parameter spaces with respect to the case in which cross-diffusion is absent. A similar effect was obtained by considering positive cross-diffusion only in the inhibitor ($d_\theta = 0$). As a result, the specific role of cross-diffusion on activator or on inhibitor emerged very clearly with respect to the system capability to promote Turing instability.

The present study shows that this same specificity emerges, even more markedly, with respect to the system capability to support Turing-Hopf instability. We find in fact that, when cross-diffusion in the η component only is considered ($d_\eta = 0$), a very large range of the cross-diffusion coefficients d_θ makes the emergence of the TH instability possible. On the contrary, when cross-diffusion in the θ component only is considered ($d_\theta = 0$), TH instability can occur only for a very small range of the cross-diffusion coefficient d_η.

This would suggest that, for an activator-inhibitor system, TH instability could be more easily detectable for models exhibiting cross-diffusion in the activator component. We stress that this circumstance is not particularly pronounced for the Strong TH instability, that we were able to find numerically for the cases of cross-diffusion in the activator as well as in the inhibitor. On the contrary, the Weak TH instability - although theoretically possible in both the previous situations - was captured numerically only when cross-diffusion in the activator is considered and, more precisely, only for values of the cross-diffusion coefficient d_θ sufficiently large.

A further difference between Weak and Strong TH instabilities, can be expressed in terms of the effective domain size required for the occurrence of these two phenomenologies. In the case of Strong TH, the effective domain size has to be larger than a critical value $\mathcal{A}^*$ that resulted: (i) independent on the cross-diffusion coefficients but only dependent on the parameter d and C; (ii) considerably larger if compared to the values of $\mathcal{A}$ for which Weak TH can emerge. In fact, for

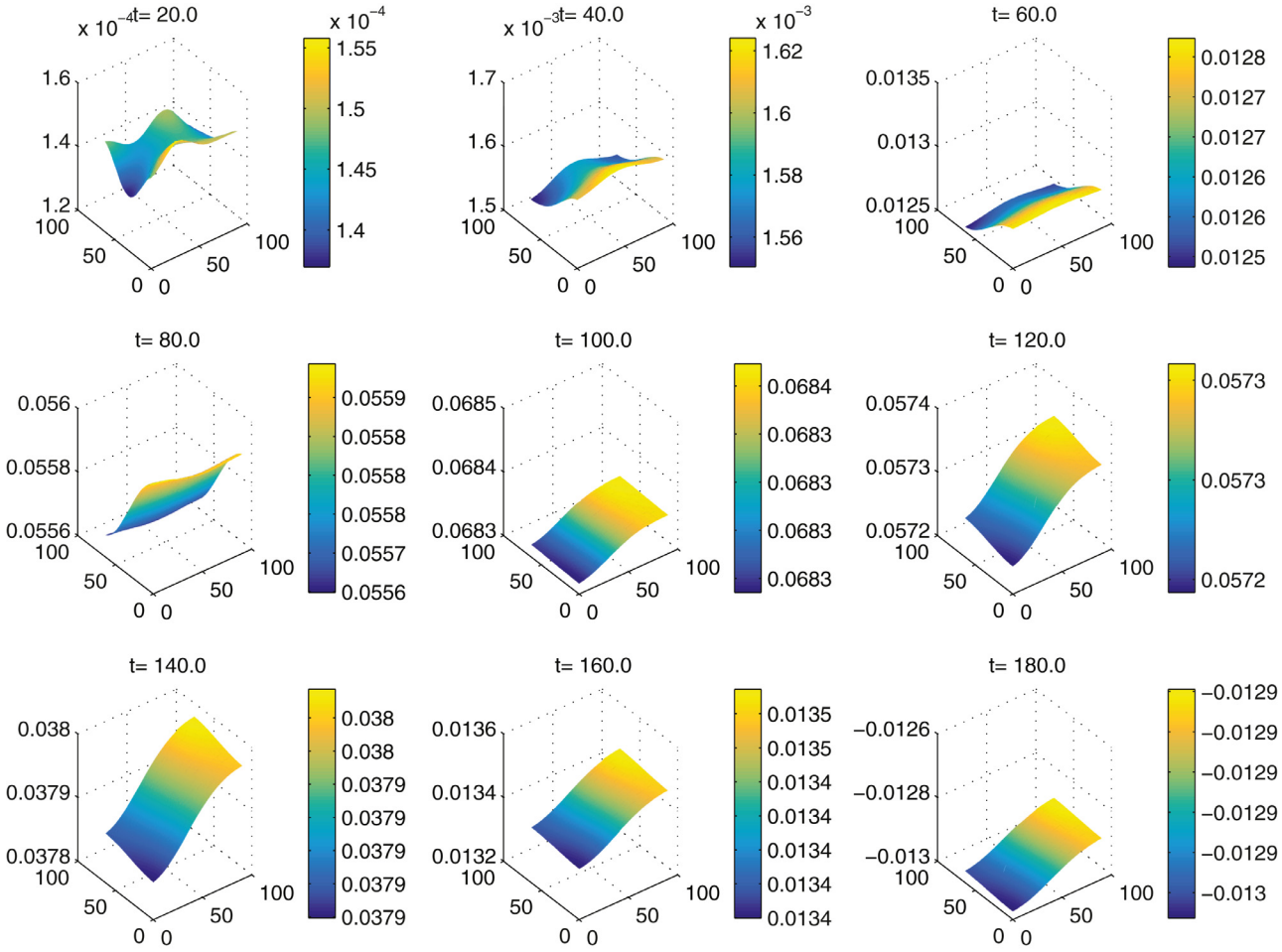

Fig. 3. Cross-diffusion in the η component only, i.e. $d_\eta = 0$, $d_\theta = 20$. **Weak TH instability** obtained for $C = 2.794$ and $B = 67.2$. Here $L_x = 2$, $L_y = 1$, $\rho = 1.6250$. (a) Snapshots of 3D spatial patterns: oscillations in time of a stationary spatial pattern can be recognized by the colorbars and by comparing the spatial structures in each snapshot (b) Left panel: spatially averaged value $< \eta >$ and $< \theta >$ as a function of time. Right panel: the corresponding oscillatory dynamics in the $(< \eta >, < \theta >)$ phase plane.

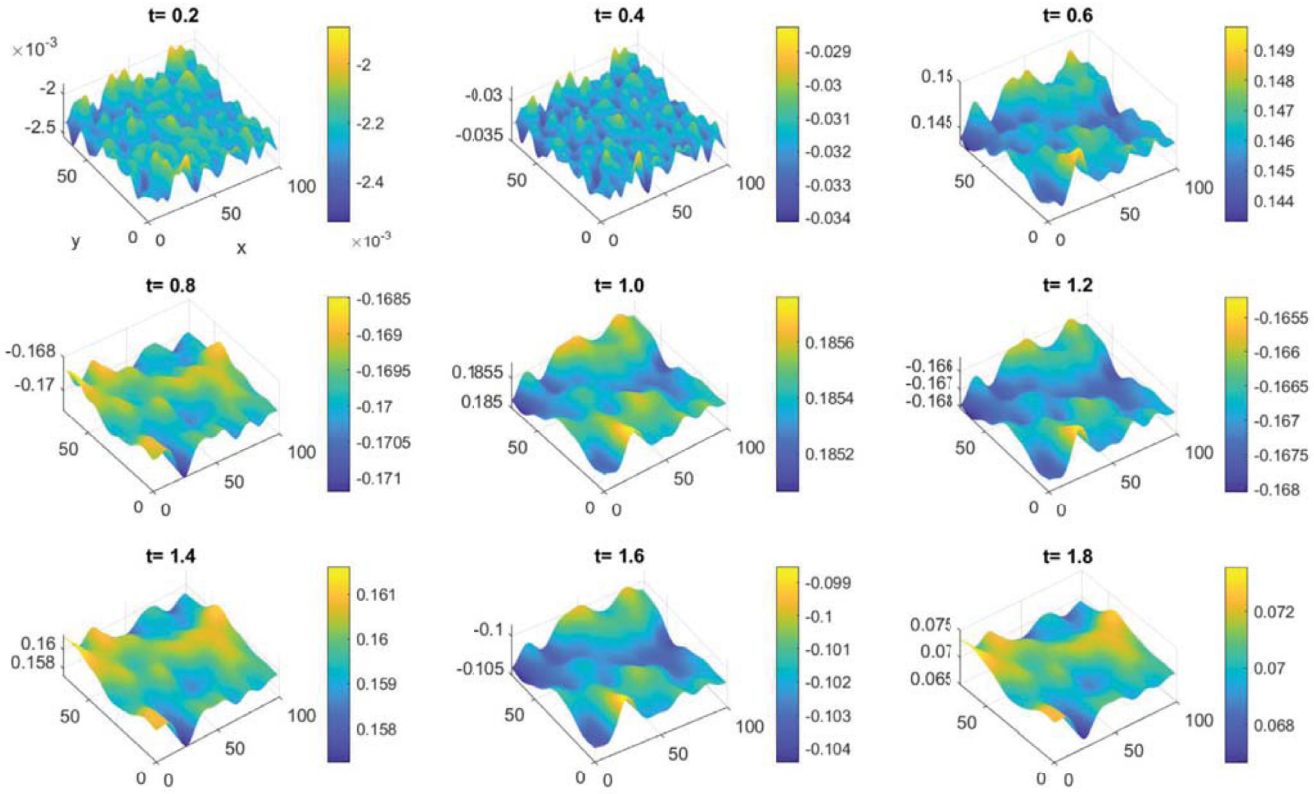

(a)

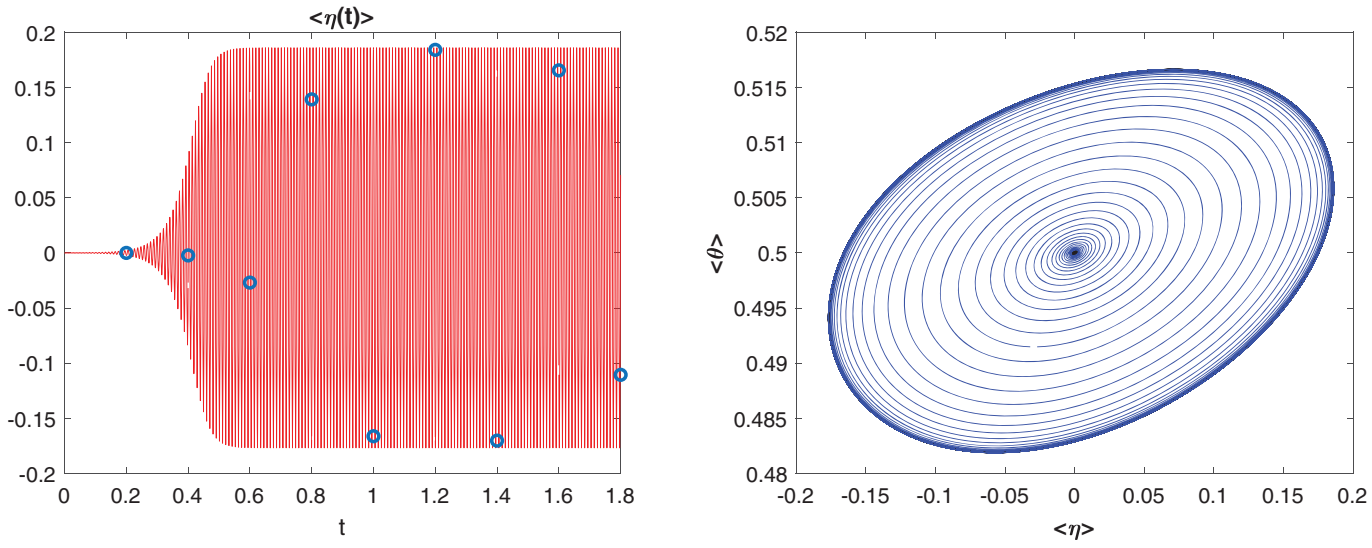

(b)

Fig. 4. Cross-diffusion in the θ component only, i.e. $d_\theta = 0$, $d_\eta = 0.1$. **Strong TH instability** obtained for $C = 2.794$ and $B = 136$. Here $L_x = 100$, $L_y = 70$, $\rho = 50$. (a) Snapshots of 3D spatial patterns: oscillations both in space and in time can be recognized by the colorbars and by comparing the spatial structures in each snapshot (b) Left panel: spatially averaged value $< \eta >$ as a function of time. Right panel: the corresponding oscillatory dynamics in the $(< \eta >, < \theta >)$ phase plane. The symbols $'o'$ indicate the points $(t_i, \langle \eta(t_i) \rangle), i = 1, \ldots, 9$ corresponding to the patterns in (a) for the same time values. In particular, note that for $t = 1.2$ and $t = 1.4$, a maximum and a minimum in $\langle \eta(t) \rangle$ correspond to the complementary patterns as shown in (a), thus emphasizing the typical Strong TH behaviour of the solution.

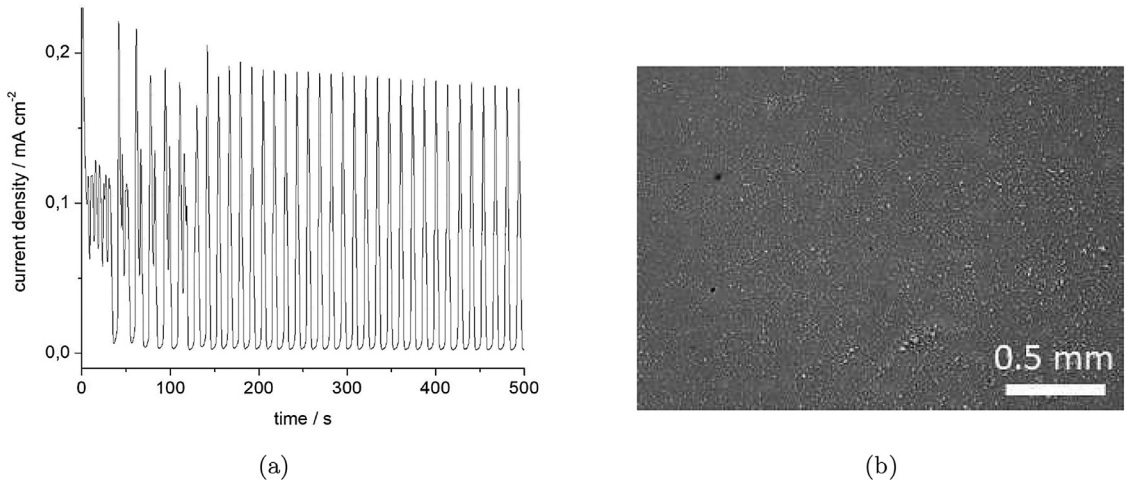

(a) (b)

Fig. 5. (A) Current-density time-series, obtained with a Zn electrode in contact with a 6 M KOH aqueous solution, polarized potentiostatically at -1018 mVHg/HgO. (B) Typical scanning-electron micrograph of a Zn electrode subjected to the conditions leading to the electrochemical behaviour depicted in Panel (A).

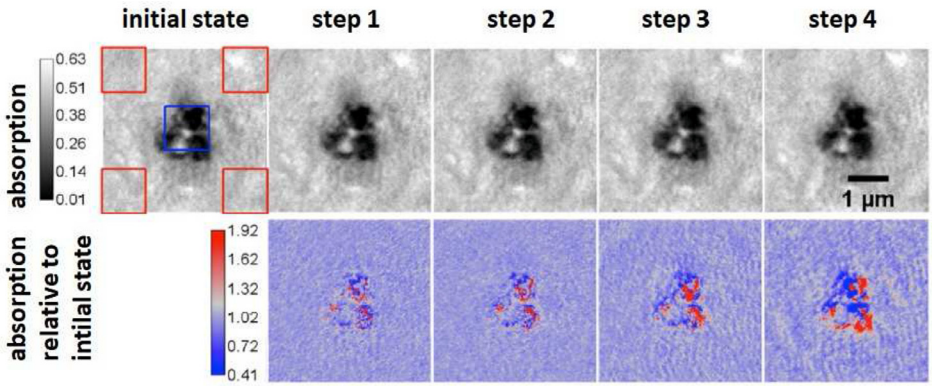

(a)

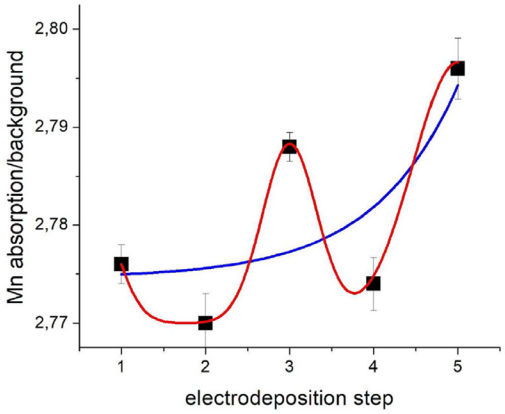

(b)

Fig. 6. (A) Upper panel: in situ soft-X ray electrochemical imaging of the growth of a single Mn-Co/polypyrole island. Lower panel: absorption ratio relative to the initial state. In this case, the background-normalized absorption is proportional to the amount of Mn deposited. (B) Black squares: measured amount of material deposited in successive electrodeposition steps (mean and standard deviation); blue line: growth trend of electrodeposited island; red line: a guide for the eye highlighting that global growth goes through oscillations in the amount of instantaneously deposited material. Panel (A) is adapted by permission from Springer Nature Customer Service Centre GmbH: Springer Nature, Nano Research, 'Shedding light on electrodeposition dynamics tracked in situ via soft X-ray coherent diffraction imaging', G. Kourousias, B. Bozzini, A. Gianoncelli, M.W.M. Jones, M. Junker, G. van Riessen, M. Kiskinova, Nano Research 9 (2016) 2046-2056 ©.

Weak TH instability to appear, the value of the effective domain size must belong to a bounded interval whose size depends on the cross-diffusion parameters (increasing with increasing d_θ and decreasing with increasing d_η). Although for rather binding values of the effective domain size, the introduction of cross-diffusion would therefore seem to make the Weak TH easier to find. The Weak TH instability exhibits in fact a less easily detectable phenomenology with respect to the Strong TH that appears instead more influenced by diffusion and kinetics mechanisms. In this respect, it is worth to stress that, for the DIB model without cross-diffusion, we theoretically predicted in Lacitignola et al. (2015) the emergence of the Weak TH instability although it was not possible to show numerically this phenomenology. The introduction of cross-diffusion in the DIB model allowed us to provide such an example. The cross-diffusion mechanism seems in fact to have increased the capability of the system to express this behavior by enlarging the range of the parameter values required for the Weak TH instability to occur and, likely, by increasing the stability of the resulting spatio-temporal patterns.

We would like to extend the present study based on cross-diffusion effects to solve the DIB model on surfaces, as done in the case of the

sphere in Lacitignola et al. (2017, 2019). In this case, a suitable numerical method would be applied to solve RD with cross-diffusion on fixed and evolving surfaces, like the Lumped surface finite element method (LSFEM) studied in Frittelli et al. (2017). Experimental evidence is available of both weak and strong Turing-Hopf instabilities. In the following we report two representative cases, measured by the Authors. Potentiostatic current oscillations observed in conditions close to pseudo-passivation of zinc electrodes (Fig. 5-A) yielding homogeneous corrosion on the mesoscopic scale (Fig. 5-B), can be modelled with weak Turing-Hops instabilities since the current is directly proportional to η.

In Kourousias et al. (2016) we observed that the single Mn-Co/polypyrole islands can grow in an oscillating mode, fully compatible with strong Turing-Hopf instability. In Fig. 6-A, we report local material redistribution resulting from consecutive in situ electrochemical growth steps, as observed by phase soft-X ray absorption imaging, together with the absorption ratio relative to the initial state, pinpointing the redistribution of material within each island. The plots of Panel B highlight that the net growth rate goes on through steps in which the amount of deposited material varies in an oscillatory way. It is worth noting that Turing-Hopf type processes are of interest for the dynamics of batteries with metallic anodes, in which oscillating space-time shape changes can take place during charge or discharge periods. Referring to the classical case of zinc anodes, oscillations under electrochemical conditions that are characteristic of charge (Nishikiori et al., 2011; Wang et al., 2003) and discharge (Bozzini et al., 2019; Chen et al., 2012; Mogi et al., 1996; Piatti et al., 1980) processes, have been described in the literature and explained on the basis of both cathodic (Despic et al., 1976) and anodic (Baugh and Baikie, 1985; Hull et al., 1970) pseudo-passivation processes, leading to alternating formation and disruption of reaction-product films at the electrode-electrolyte interface, that trigger relaxation oscillations. In Fig. 7 we report a typical example from our laboratory of potential oscillations observed during the operation at 1 mA cm^{-2} of a symmetric zinc cell with 6 M KOH, 0.1 M ZnO aqueous electrolyte, containing 0.3 mM tetrabutylammonium bromide additive. Potential oscillations of this type accompany morphology evolution that can lead to periodically changing metal pattern distributions on the electrode surface. In fact, complex morphochemical processes are generated by the reactions involved in the energy storage processes, that can modulate the electrode surface area, causing reorganizations in space and time that can be periodic in nature. For instance, the following sequences of cathodic and anodic processes can be figured out, as a simplified model of these phenomena. During charge, metal protrusions typically tend to form (Fig. 8-A), initially increasing

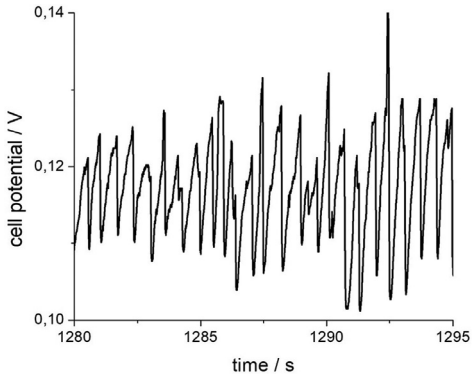

Fig. 7. A typical chunk of a cell voltage time series for a Zn/Zn symmetrical cell, polarized galvanostatically at 1 $mAcm^{-2}$. Electrolyte: 6 M KOH + 0.1 M ZnO + 0.3 mM TBAB.

the active electrode area. At later stages of growth, branched portions of the protrusion (Fig. 8-B) can detach, giving rise to 'dead metal particles' in the electrolyte, thus decreasing the active metal surface. Moreover, unstably growing metal features tend to screen the neighboring regions of the cathode, where oxide films tend to precipitate (Fig. 8-C), but their conversion back to metal can be triggered by the protrusion deactivation processes, such as the one mentioned above. Similar processes can also occur during discharge, where regions of low and high current density give rise to the formation, respectively, of soluble and insoluble forms of oxidized metal Mele et al. (2017) (Fig. 8-D), that in turn modulate the metal dissolution rate in space and time: fast reacting regions tend to passivate, increasing the reaction rate of neighboring regions that initially react slower; in addition, under appropriate conditions, the passivating film tends to fail for mechanical and chemical reasons, reactivating the underlying metal. These processes, and similar ones that are likely to occur at the surface of metal battery anode, yield coupled dynamic morphochemistry that is compatible with Turing-Hopf phenomenology.

Oscillations of integral electrical quantities, such as cell current or potential, can be readily measured, but in situ observation of dynamic morphological processes is still in its infancy. X-ray based imaging methods, based on direct- Bozzini et al. (2020) or Fourier Bozzini et al. (2017) space approaches are starting to find application and contribute unprecedented insight into the internal workings of operating electrodes. In view of an expected notable expansion of these studies,

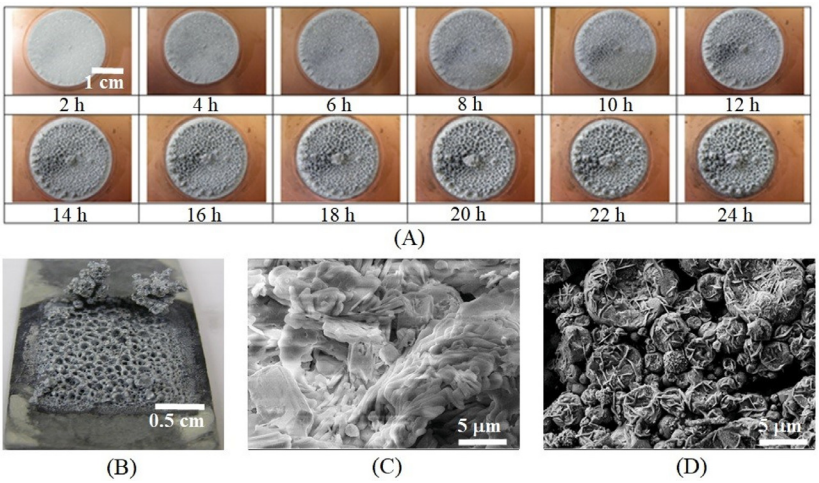

Fig. 8. Selected images of Zn electrodes, showing typical morphologies. (A) Electrodeposition from 2M ZnSO4 aqueous solution, pH 4.5 at 40 mA cm^{-2} for the indicated times. (B) Electrodeposition from 2M ZnSO4 solution, pH 4.5 at 80 mA cm^{-2} for 16 h. (C) Thick ZnO passive film obtained by exposure of a Zn electrode to a 6M KOH, 0.1M ZnO aqueous solution. (D) Surface of an electrodeposited Zn film, treated anodically in 6M KOH, 0.1M ZnO aqueous solution at -1020 $mV_{Hg/HgO}$ for 1 h.

enabled by next-generation high-throughput microspectoscopy methods being actively developed at X-ray light sources around the world, the availability of mathematical models of the practically relevant mesoscopic materials science processes, like the DIB model for battery systems in which conversion reactions are implemented, will be a necessary tool for both physico-chemical rationalization and parameter-based data compression.

Declaration of Competing Interest

The authors of the manuscript declare that they have no known competing financial interests or personal relationships that could have appeared to influence the work reported in this paper.

Acknowledgements

D.L. research work has been performed under the auspices of the Italian National Group for Mathematical Physics (GNFM-Indam). I.S. research work has been performed under the auspices of the Italian National Group for Scientific Calculus (GNCS-INdAM). We also thank the anonymous referees and the Editor for their valuable comments and remarks.

References

Amann, H., 1990. Dynamic theory of quasilinear parabolic equations. II. Reaction-diffusion systems. Differ. Integral Equ. 3 (1), 13–75.
Baugh, L., Baikie, A., 1985. Passivation of zinc in concentrated alkaline solution ii. role of various experimental factors and the distinction between the solid-state and dissolution precipitation mechanisms. Electrochimica Acta 30 (9), 1173–1183.
Bozzini, B., D'Autilia, M., Mele, C., Sgura, I., 2019. Dynamics of zinc-air battery anodes: an electrochemical and optical study complemented by mathematical modelling. La Metallurgia Italiana 111, 33–39.
Bozzini, B., Gambino, G., Lacitignola, D., Lupo, S., Sammartino, M., Sgura, I., 2015. Weakly nonlinear analysis of Turing patterns in a morphochemical model for metal growth. Comput. Math. Appl. 70 (8), 1948–1969.
Bozzini, B., Kourousias, G., Gianoncelli, A., Jones, M., Van Riessen, G., Kiskinova, M., 2017. Soft X-ray ptychography as a tool for in operando morphochemical studies of electrodeposition processes with nanometric lateral resolution. J. Electron Spectrosc. Relat. Phenomena 220, 147–155.
Bozzini, B., Lacitignola, D., Sgura, I., 2013. Spatio-temporal organization in alloy electrodeposition: a morphochemical mathematical model and its experimental validation. J. Solid State Electrochem. 17 (2), 467–479.
Bozzini, B., Mele, C., Veneziano, A., Sodini, N., Lanzafame, G., Taurino, A., Mancini, L., 2020. Morphological evolution of Zn-sponge electrodes monitored by in situ X-ray computed microtomography. ACS Appl. Energy Mater. 3, 4931–4940.
Chattopadhyay, J., Tapaswi, P.K., 1997. Effect of cross-diffusion on pattern formation – a nonlinear analysis. Acta Applicandae Mathematica 48 (1), 1–12.
Chen, A., Cao, F., Liu, W., Zheng, L., Zhang, Z., Zhang, J., Cao, C., 2012. Shot noise analysis on corrosion behavior of zinc alloy ($ZnAl_4Cu_1$) under dry-wet cycles. Trans. Nonferrous Metals Soc. China 22 (1), 228–240.
Cross, M., Greenside, H., 2009. Pattern Formation and Dynamics in Nonequilibrium Systems. Cambridge University Press, Cambridge.
De Wit, A., 1999. Spatial patterns and spatiotemporal dynamics in chemical systems. Adv. Chem. Phys. 109, 435–513.
De Wit, A., Lima, D., Dewel, G., Borckmans, P., 1996. Spatiotemporal dynamics near a codimension-two point. Phys. Rev. E 54, 261–271.
Despic, A., Jovanovic, D., Rakic, T., 1976. Kinetics and mechanism of deposition of zinc from zincate in concentrated alkali hydroxide solutions. Electrochimica Acta 21 (1), 63–77.
Frittelli, M., Madzvamuse, A., Sgura, I., Venkataraman, C., 2017. Lumped finite elements for reaction cross-diffusion systems on stationary surfaces. Comput. Math. Appl. 74 (12), 3008–3023.
Gambino, G., Lombardo, M., Lupo, S., Sammartino, M., 2016. Super-critical and sub-critical bifurcations in a reaction-diffusion Schnakenberg model with linear cross-diffusion. Ricerche di Matematica 1–19.
Hull, M., Ellison, J., Toni, J., 1970. The anodic behavior of Zinc electrodes in potassium hydroxide electrolytes. J. Electrochem. Soc. 117, 192–198.
Kourousias, G., Bozzini, B., Gianoncelli, A., Jones, M., Junker, M., Van Riessen, G., Kiskinova, M., 2016. Shedding light on electrodeposition dynamics tracked in situ via soft X-ray coherent diffraction imaging. Nano Res. (Springer) 9, 2046–2056.
Lacitignola, D., Bozzini, B., Frittelli, M., Sgura, I., 2017. Turing pattern formation on the sphere for a morphochemical reaction-diffusion model for electrodeposition. Commun. Nonlinear Sci. Numer. Simul. 48, 484– 508.
Lacitignola, D., Bozzini, B., Peipmann, R., Sgura, I., 2018. Cross-diffusion effects on a morphochemical model for electrodeposition. Appl. Math. Model. 57, 492– 513.
Lacitignola, D., Bozzini, B., Sgura, I., 2014. Spatio-temporal organization in a morphochemical electrodeposition model: analysis and numerical simulation of spiral waves. Acta Applicandae Mathematicae 132, 377–389.
Lacitignola, D., Bozzini, B., Sgura, I., 2015. Spatio-temporal organization in a morphochemical electrodeposition model: Hopf and Turing instabilities and their interplay. Eur. J. Appl. Math. 26 (2), 143–173.
Lacitignola, D., Sgura, I., Bozzini, B., Dobrovolska, T., Krastev, I., 2019. Spiral waves on the sphere for an alloy electrodeposition model. Commun. Nonlinear Sci. Numer. Simul. 79, 104930.
Madzvamuse, A., Barreira, R., 2014. Exhibiting cross-diffusion-induced patterns for reaction-diffusion systems on evolving domains and surfaces. Phys. Rev. E 90, 043307.
Madzvamuse, A., Ndakwo, H., Barreira, R., 2015. Cross-diffusion-driven instability for reaction-diffusion systems: analysis and simulations. J. Math. Biol. 70, 709–743.
Mele, C., Bilotta, A., Bocchetta, P., Bozzini, B., 2017. Characterization of the particulate anode of a laboratory flow Zn-Air fuel cell.. J. Appl. Electrochem. 47, 877–888.
Miller, D., Vitagliano, V., Sartorio, R., 1986. Some comments on multicomponent diffusion: negative main term diffusion coefficients, second law constraints, and reference frame transformations.. J. Chem. Phys. 90, 1509–1519.
Mogi, I., Kikuya, H., Watanabe, K., Awaji, S., Motokawa, M., 1996. Magnetic field effects on the current oscillations in anodic zinc dissolution. Chem. Lett. 25 (8), 673–674.
Murray, J., 2003. Mathematical Biology II - Spatial Models and Biomedical Applications. Springer-Verlag, Berlin Heidelberg.
Mutoru, W.J., Firoozabadi, A., 2011. Form of multicomponent Fickian diffusion coefficients matrix. J. Chem. Thermodyn. 43 (8), 1192–1203.
Nishikiori, R., Morimoto, S., Fujiwara, Y., Tanimoto, Y., 2011. Magnetic field effect on the cathodic potential oscillation of zinc electrode in alkaline solutions. Appl. Magn. Reson. 41, 221–227.
Piatti, R., Podest, J., Arva, A., 1980. Characteristics of the periodic faradaic current oscillations of zn/alkaline solution interfaces under potentiostatic conditions. Electrochimica Acta 25 (6), 827–831.
Ricard, M.R., Mischler, S., 2009. Turing instabilities at HOPF bifurcation. J. Nonlinear Sci. 19 (5), 467–496.
Rudovics, B., Dulos, E., de Kepper, P., 1996. Standard and nonstandard turing patterns and waves in the CIMA reaction. Physica Scripta T67, 43–50.
Settanni, G., Sgura, I., 2016. Devising efficient numerical methods for oscillating patterns in reaction-diffusion systems. J. Comput. Appl. Math. 292 (C), 674–693.
Sgura, I., Bozzini, B., Lacitignola, D., 2012. Numerical approximation of Turing patterns in electrodeposition by ADI methods. J. Comput. Appl. Math. 236 (16), 4132–4147.
Sherratt, J., 2012. Turing patterns in deserts. In: Cooper, S.B., Dawar, A., Lowe, B. (Eds.), How the World Computes. Springer, New York. Lecture Notes in Computer Science 7318
Smoller, J., 1994. Shock Waves and Reaction-Diffusion Equations. Springer Science & Business Media, New York.
Turing, A.M., 1952. The chemical basis of morphogenesis. Philos. Trans. R. Soc. Lond. B: Biol. Sci. 237 (641), 37–72.
Vanag, V.K., Epstein, I.R., 2009. Cross-diffusion and pattern formation in reaction-diffusion systems. Phys. Chem. Chem. Phys. 11, 897–912.
Wang, S., Zhang, K., Xu, Q., Wang, M., Peng, R., Zhang, Z., Ming, N., 2003. Oscillations in electrochemical deposition of ZINC. J. Phys. Soc. Jpn. 72, 1574–1580.
Wang, X., Cai, Y., 2013. Cross-diffusion-driven instability in a reaction-diffusion Harrison predator-prey model. Abstract Appl. Anal. 2013, 1–9.